

Fast mixed-species quantum logic gates for trapped-ion quantum networks

Zain Mehdi,^{1,*} Varun D. Vaidya,² Isabelle Savill-Brown,¹ Phoebe Grosser,¹ Alexander K. Ratcliffe,² Haonan Liu,² Simon A. Haine,¹ Joseph J. Hope,¹ and C. Ricardo Viteri²

¹*Department of Quantum Science, Research School of Physics, Australian National University*

²*IonQ, Inc., College Park, MD, USA*

(Dated: December 11, 2024)

Quantum logic operations between physically distinct qubits is an essential aspect of large-scale quantum information processing. We propose an approach to high-speed mixed-species entangling operations in trapped-ion quantum computers, based on mechanical excitation of spin-dependent ion motion by ultrafast pulsed lasers. We develop the theory and machine-design of pulse sequences that realise MHz-speed ‘fast gates’ between a range of mixed-isotope and mixed-species ion pairings with experimentally-realistic laser controls. We demonstrate the robustness of the gate mechanism against expected experimental errors, and identify errors in ultrafast single-qubit control as the primary technical limitation. We demonstrate that the mixed-species fast gate mechanism enables the protection of ion-photon entanglement against rapid spin dephasing of matter-photon interfaces, paving the path for high-fidelity and high-speed quantum networking in trapped-ion architectures.

Introduction.— In trapped-ion systems, mixed-species quantum logic operations allow coherent mapping of quantum information between quantum memories, logical qubits and ancilla qubits [1–6], which underpins a wide range of applications [2, 4, 7]: mid-circuit measurement and feedback for quantum error correction [8], shuttling-based quantum gate teleportation [9], low-excitation transport of qubits between segmented trapping zones [2, 10], and quantum logic spectroscopy [2]. Mixed-species entangling operations are particularly important for realising distributed quantum computing with highly-connected optical networks of trapped-ion quantum processing nodes (QPNs) [1, 5, 11–14]: coherent mapping between distinct network and memory qubits enables trapped-ion quantum networks to be scaled up without slowing down communication rates [13, 15].

Entangling gates between mixed-isotope and mixed-element species have previously been demonstrated using optical fields to provide qubit-state-dependent forcing of spectroscopically-resolved vibrational modes of the ion crystal [2–6, 8, 13, 15]. While these approaches are reaching fidelities comparable to state-of-the-art same-species gates (Ref. [6] achieved a two-qubit gate fidelity of 99.8%), these gate mechanisms are limited to the weak-coupling (i.e. Lamb-Dicke) regime which precludes high-fidelity two-qubit gates with operation times significantly faster than the motion of the ions [16]. This limits typical entangling rates by spectroscopic gate protocols (such as the Mølmer-Sørensen [17] and Cirac-Zoller schemes [18]) to $\mathcal{O}(10)$ kHz [19], with longer operation times required for error-robust schemes [20, 21]. These limitations are exacerbated for mixed-species crystals with significant mass imbalances ($\gtrsim 10\%$) [22], as well as for long-ion chains with crowded motional spectra [20, 21, 23, 24]. Overcoming these existing gate speed limitations is critical for realising large-scale computation in modular trapped-ion networks, which hinges on the ability to coherently map quantum information between

atomic memories and ‘network’ qubits used to interface with photonic links [1]. In order to retain high-fidelity quantum logic between QPNs, multi-species gate operations must be orders of magnitude faster than the typical network-qubit dephasing rates of 1 – 10 kHz [2, 3, 5, 13].

In this Letter, we propose an alternative approach to mixed-species quantum logic operations based on mechanical excitation of ion motion using impulsive spin-dependent kicks (SDKs) on nanosecond timescales. We identify high-fidelity gate solutions for a range of experimentally-relevant species pairings, demonstrating that high-fidelity two-qubit operations can be performed in hundreds of nanoseconds with tens of impulsive SDKs and experimentally-accessible laser repetition rates. We demonstrate that the mixed-species fast gate protocol enables high-fidelity SWAP gates between short-lived Zeeman qubits and long-lived hyperfine qubits, which paves the path for high-speed and high-fidelity quantum networks of trapped-ion qubits connected by photonic links.

Theory of mixed-species fast gates.— Here we develop the theory of fast entangling gates between mixed-species ion pairs, based on SDKs delivered to each ion by counter-propagating π -pulse pairs. This mechanism has been extensively studied for same-species crystals [25–35] and Bell-state preparation has been experimentally demonstrated with two $^{171}\text{Yb}^+$ ions (in $20\mu\text{s}$ and 76% fidelity) [36]. The mixed-species protocol is distinguished from same-species approaches by allowing for SDKs to be implemented on different transitions for each of the two ions: $\hat{U}_{\text{SDK}}(k^{(1)}, k^{(2)}) = \prod_{j=1,2} \hat{U}_{\pi}^{(j)}(k^{(j)}) \hat{U}_{\pi}^{(j)}(-k^{(j)})$, where $\hat{U}_{\pi}^{(j)}(k) = \hat{\sigma}_x^{(j)} e^{ik^{(j)} \hat{x}^{(j)} \hat{\sigma}_z^{(j)}}$ is the unitary for an ideal π -pulse delivered to the j -th ion with transition wavelength $\lambda^{(j)} = (2\pi)/k^{(j)}$.

The fast gate mechanism consists of impulsive SDKs (taken to be effectively instantaneous with respect to the ion motion), interspersed by free evolution of the ions [37]. We will allow for the direction of the pulses

to be switched, described by inverting the sign of the wavevectors, i.e. $\hat{U}_{\text{SDK}}(-k^{(1)}, -k^{(2)})$, such that SDKs arriving at times $\{t_m\}$ are described by wavevectors $z_m k^{(j)}$ where $z_m = \pm 1$ describes the direction of the m -th kick. The total unitary for the gate evolution is then $\hat{U}_{\text{G}} = \prod_m \hat{U}(t_{m+1} - t_m) \hat{U}_{\text{SDK}}(z_m k^{(1)}, z_m k^{(2)})$. Up to a global phase, this is equivalent to the expression [37]

$$\hat{U}_{\text{G}} = e^{i\Theta} e^{i\sigma_z^{(1)} \sigma_z^{(2)}} \prod_{\alpha=1}^L \hat{D}_{\alpha}(\beta_{\alpha}^{(1)} \hat{\sigma}_z^{(1)} + \beta_{\alpha}^{(2)} \hat{\sigma}_z^{(2)}), \quad (1)$$

where $\beta_{\alpha}^{(j)} = 2i\eta_{\alpha}^{(j)} b_{\alpha}^{(j)} \sum_m z_m e^{i\omega_{\alpha} t_m}$ characterises the final motional state of each mode ($\hat{D}_{\alpha}(\beta)$ is the displacement operator on mode α with amplitude β). Here \vec{b}_{α} and ω_{α} are respective eigenvector and secular eigenfrequency of the α -th motional mode, and $\eta_{\alpha}^{(j)} \equiv k^{(j)} \sqrt{\hbar/(2m^{(j)}\omega_{\alpha})}$ is the corresponding ion-dependent Lamb-Dicke parameter with $m^{(j)}$ as the j -th ion's mass. The two-qubit phase Θ in Eq. (1) is given by [37]:

$$\Theta = 8 \sum_{\alpha} b_{\alpha}^{(1)} b_{\alpha}^{(2)} \eta_{\alpha}^{(1)} \eta_{\alpha}^{(2)} \sum_{m=2}^{\mathcal{N}} \sum_{n=1}^{m-1} z_n z_m \sin(\omega_{\alpha} \delta t_{mn}) \quad (2)$$

for $\delta t_{mn} \equiv t_m - t_n$ and \mathcal{N} total SDKs. Provided the motional states are restored at the end of the gate operation (i.e. $\beta_{\alpha}^{(j)} = 0$), Eq. (1) realises a $\hat{\sigma}_z \otimes \hat{\sigma}_z$ phase gate, which is maximally entangling when $\Theta = \pi/4$. We note that the derivation of Eqs. (1) and (2) does not make use of a weak-coupling approximation (see Supplementary Material [37]), such that the gate mechanism is performant outside the Lamb-Dicke regime (distinctive from spectroscopic gate mechanisms [19]).

Imperfect phase accumulation ($\Theta \neq \pi/4$) and imperfect motional restoration ($\beta_{\alpha}^{(j)} \neq 0$) contributes to a non-zero gate error that can be quantified by the state-averaged infidelity [37]:

$$\frac{3}{2} \varepsilon_{\text{av}} = |\Delta\Phi|^2 + \sum_{\alpha} \left(\bar{n}_{\alpha} + \frac{1}{2} \right) (|\beta_{\alpha}^{+}|^2 + |\beta_{\alpha}^{-}|^2), \quad (3)$$

where $\Delta\Phi = \Theta - \pi/4$, \bar{n}_{α} is the mean thermal occupancy of each mode prior to the gate, and $\beta_{\alpha}^{\pm} = \beta_{\alpha}^{(2)} \pm \beta_{\alpha}^{(1)}$. Note that for perfect motional restoration, $\beta_{\alpha}^{\pm} = 0$, the fast gate mechanism is completely insensitive to the temperature of the system. Unless otherwise stated, we assume a constant mode occupation of $\bar{n}_{\alpha} = 1$ for all calculations presented in this work, which gives roughly equal contributions of motional and phase errors to the total gate error.

In this work, we design SDK sequences that minimize the intrinsic gate error given by Eq. (3) by use of a two-stage machine design procedure [30], summarized in Appendix A. The objective of this minimization is to find an SDK sequence that realizes a high-fidelity maximally-entangling gate of a target operation time τ_{G} with the

fewest number of SDKs, \mathcal{N} . This is achieved by bounding \mathcal{N} in each gate search, and iteratively increasing this bound until a solution is found with state-averaged fidelity above 99.9% ($\varepsilon_{\text{av}} \leq 10^{-3}$). Furthermore, we impose a bandwidth limit of 200 MHz on the SDK sequence, which is well-within the capability of existing ultrafast laser controls on both hyperfine qubits [38–40] and Zeeman qubits [41].

Results.— Here we demonstrate the applicability of the fast gate mechanism to a wide range of mixed-species pairs by considering gates between a number of different experimental pairings relevant to quantum networking: ^{133}Ba – ^{138}Ba [42, 43], ^{43}Ca – ^{88}Sr [6, 13, 44], and ^{43}Ca – ^{40}Ca [45]. Each pairing contains a hyperfine qubit and Zeeman qubit, such that the former can be used as a quantum memory and the latter can be used for photonic interfaces [1, 11]. We also consider fast gates between the unusual pair ^{171}Yb – ^9Be , to demonstrate that the fast gate mechanism is performant for large mass-imbalance pairs, which are highly limiting for spectroscopic gate protocols [22].

In each case, we assume the hyperfine/Zee-man qubits are stored in the $s_{1/2}$ ground-state manifold, and that SDKs are implemented on the axial modes of the trap using two-photon Raman transitions. We assume individual addressing of each ion using a pair of counter-propagating Raman beams tilted at an angle of $\theta = \pi/4$ from the longitudinal axis of the trap [see Fig. 2(c)] such that each the effective wavevector of the two-photon transition is $k_{\text{eff}}^{(j)} = \pm\sqrt{2}k^{(j)}$. We will provide an explicit example of a SDK implementation for the ^{133}Ba – ^{138}Ba pairing later in this manuscript. For concreteness, we assume the hyperfine qubit experiences a trapping frequency $\omega_{0,\text{H}} = 2\pi \times 1\text{MHz}$; due to the mass-dependence of the RF-pseudopotential, the Zeeman qubit will experience a trapping frequency of $\omega_{0,\text{Z}} = \omega_{0,\text{H}} \sqrt{m^{(\text{H})}/m^{(\text{Z})}}$.

Figure 1(a) presents gate solutions that have state-averaged fidelities above 99.9% before the inclusion of errors in the SDKs, and demonstrates that sub-microsecond gate speeds are achievable with small numbers of SDKs ($\mathcal{N} \sim 5 - 30$) across all mixed-species pairs considered. This is a significant improvement over previous theoretical work that reported a significantly larger number of pulses ($\mathcal{N} \sim 50$) to achieve similar gate times [30, 32]. This further advances prospects for experimental realisation of fast gates: Ref. [36] used 10 SDKs to experimentally demonstrate a $20\mu\text{s}$ entangling operation. Fig. 1(a) demonstrates that an order of magnitude increase in gate speed can be achieved using similar numbers of SDKs. The fastest gate solutions are found for the high-mass-imbalance pair, ^{171}Yb – ^9Be , with gate operation times as low as 300ns achievable with $\mathcal{N} \geq 25$ SDKs.

For pairings of ^{43}Ca – ^{88}Sr and ^{43}Ca – ^{40}Ca , Fig. 1(a) demonstrates that MHz-speed gates are achievable with as few as 5–10 SDKs. We find a $1.8\mu\text{s}$ gate solu-

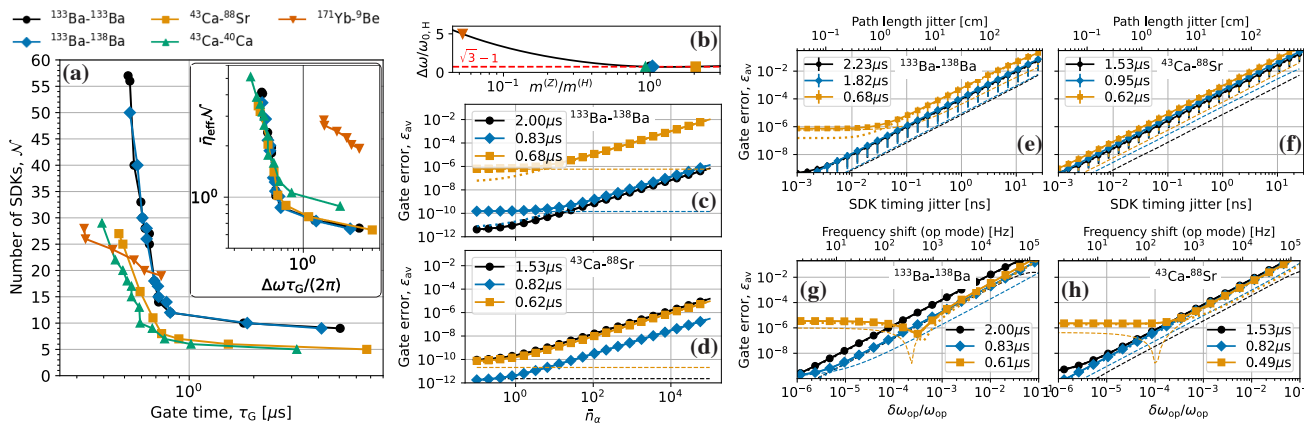


FIG. 1. (a) Fast gate solutions with state-averaged fidelities above 99.9%, assuming idealised SDKs, demonstrating a trade-off between the gate time (τ_G) and number of SDKs (\mathcal{N}). Inset: A universal trend is revealed under the rescaling $\mathcal{N} \rightarrow \bar{\eta}_{\text{eff}}\mathcal{N}$, $\tau_G \rightarrow \Delta\omega\tau_G/(2\pi)$, with the exception of the large-mass-imbalance pair $^{171}\text{Yb}-^9\text{Be}$. (b) Frequency splitting between the out-of-phase (op) and in-phase (ip) motional modes, $\Delta\omega$. (c-d) Dependence of the gate error on the mode occupation, including contributions from the phase error (dashed line) and motional error (dotted line), for select gate solutions of (c) $^{133}\text{Ba}-^{138}\text{Ba}$ and (d) $^{43}\text{Ca}-^{88}\text{Sr}$ ion pairings. (e-f) Sensitivity of select gate solutions against timing jitter in the SDK pulse sequence, with the gate error averaged over 10^4 noise realisations. Errorbars indicate the standard deviation in the ensemble average. (g-h) Impact of frequency drifts of the high-frequency op mode on the state-averaged gate error, for select gate solutions.

tion with only $\mathcal{N} = 5$ SDKs for the pair $^{43}\text{Ca}-^{88}\text{Sr}$ (see Appendix A), which is promising for near-term experimental demonstrations (see discussion on imperfect SDKs below). A modest increase to $\mathcal{N} \approx 20$ SDKs enables high-fidelity gate solutions with minimal intrinsic error and operation speeds below 500ns for both of these pairings. This is comparable to the fastest two-qubit gate experimentally demonstrated on trapped-ion systems 480ns [16], which was subject to large errors ($\sim 40\%$) due to out-of-Lamb-Dicke-regime effects [46]. In contrast, the fast gate mechanisms based on impulsive SDKs do not require operation in the Lamb-Dicke regime – Fig. 1(c-d) demonstrates gate errors below 10^{-6} are achievable even under large phonon occupations of $\bar{n} \sim 10^3 - 10^4$, as gate solutions with vanishingly small motional restoration errors ($\sim 10^{-11}$) are accessible for a range of gate times around a microsecond.

The inset in Fig. 1(a) indicates that distinct (τ_G, \mathcal{N}) trends for each mixed-species pair collapse onto a universal tendency under the rescaling $\mathcal{N} \rightarrow \bar{\eta}_{\text{eff}}\mathcal{N}$, $\tau_G \rightarrow \Delta\omega\tau_G/(2\pi)$, where $\bar{\eta}_{\text{eff}}^2 = |b^{(1)}b^{(2)}|\eta^{(1)}\eta^{(2)}$ characterises the effective SDK coupling to the ion pair (*c.f.* Eq. (2)), and $\Delta\omega = \omega_{\text{op}} - \omega_{\text{ip}}$ is the frequency splitting between the out-of-phase (op) and in-phase (ip) motional modes of the two-ion crystal – shown in Fig. 1(b). Specifically, solutions with gate operation times $\tau_G \ll 2\pi/\Delta\omega$ collapse onto the same curve. The only ion pair to deviate from this universal trend is $^{171}\text{Yb}-^9\text{Be}$, which has distinct motional trajectories due to the large frequency splitting of $\Delta\omega/\omega_{0,\text{H}} \approx 5$ (the other pairs considered fall close to the same-species result, $\Delta\omega/\omega_0 = \sqrt{3} - 1$). This is highlighted in the motional trajectories of an exem-

plary sub-microsecond gate between $^{171}\text{Yb}-^9\text{Be}$ shown in Appendix A, where there are many oscillations of the high-frequency op mode (6.21MHz) during a 560ns gate operation, while there is only a single oscillation of the low-frequency ip mode (1.22MHz) in the same duration.

Fast gate robustness.— Next, we consider the robustness of the mixed-species fast gate mechanism against expected experimental errors.

(1) *Timing jitter.* We model timing jitter on the SDK sequence by adding Gaussian random noise to the timing of each pulse while enforcing a minimum pulse separation of 5ns (corresponding to a SDK train bandwidth of 200MHz). Fig. 1(e-f) demonstrates timing jitters of $\lesssim 1$ ns contribute errors of $\mathcal{O}(10^{-4})$ for MHz-speed mixed-species gates for the $^{133}\text{Ba}-^{138}\text{Ba}$ and $^{43}\text{Ca}-^{88}\text{Sr}$ pairs, with similar results for other ion pairings [37]. Given the sub-picosecond timing stability of ultrafast pulsed lasers [47], pulse timing errors are most likely to arrive due to optical path-length variations. As 100ps timing jitter corresponds to roughly 3cm path-length, we conclude the fast gate protocols presented here are robust to SDK timing noise. In the Supplemental Material [37], we additionally show that the fast gate schemes presented in this work are insensitive to large ($\gtrsim 10\%$) drifts in the SDK repetition rate.

(2) *Stray fields.* Next we consider the effects of stray electric fields, which can alter the secular frequencies of the RF-pseudopotential and cause mode-dependent shifts in the motional spectra of the system, thereby disturbing the motional dynamics of the gate operation. We assume drifts in the motional mode frequencies are

slow with respect to the MHz gate speeds, such that the effect of stray fields can be modelled as a systematic shift in the mode frequencies. We consider two cases: mode-dependent drift of the op mode (holding the ip mode frequency constant), and frequency drifts common to both the ip and op modes. For the former case, Fig. 1(g-h) demonstrates that frequency drifts of $\mathcal{O}(1)$ kHz induce errors of roughly 10^{-4} for a range of MHz-speed gates, with similar results observed for frequency drifts common to both modes [37]. Thus, high-fidelity fast gates require trap frequencies to be stabilised at the 0.1% level, which is readily achievable in existing microfabricated traps [48].

(3) *Imperfect SDKs.* Errors in the effective pulse area of each ultra-fast π -pulse introduce two-qubit gate errors that compound with \mathcal{N} [30]. Assuming SDK errors compound maximally, the fidelity of a gate with \mathcal{N} imperfect SDKs is bounded by $\mathcal{F}(\epsilon_\pi) \geq (1 - \mathcal{N}\epsilon_\pi)^2 \mathcal{F}_0$, where ϵ_π is the characteristic population transfer error of a single ultrafast π -pulse, and \mathcal{F}_0 is the gate fidelity in the absence of pulse errors [30, 49]. As current experiments with ultrafast pulses achieve population transfer errors of $\mathcal{O}(1\%)$ [41, 50], near-term demonstrations of the fast gate mechanism should use gate solutions with as few SDKs as possible in order to achieve high fidelities. For the $1.8\mu\text{s}$ gate between ^{43}Ca – ^{88}Sr shown in Fig. A1 (Appendix A), only $\mathcal{N} = 5$ SDKs are required, and thus can be realised with a two-qubit gate fidelity of $\approx 93\%$ with current state-of-the-art SDK errors of $\epsilon_\pi \approx 7 \times 10^{-3}$ [51]. For sub-microsecond gates with $\mathcal{N} \sim 10$, the above error model predicts gate errors of 10 – 20%. Numerical simulations indicate SDK fidelities of 99.99% are achievable with current SDK schemes [39], which would enable MHz-speed mixed-species (and same-species) entangling gates above the $\approx 99\%$ minimum threshold for fault-tolerant computing [52], and for large-scale computation in trapped-ion networks [53].

(4) *Motional heating.* Decoherence of the motional modes due to heating from electric field is a leading error source in all current entangling gate mechanisms, for both same-species [19] and mixed-species gates [2, 3, 6, 13]. MHz-speed fast entangling gates based on SDKs are only sensitive to individual heating events during the gate operation [28], which allows us to make the order of magnitude estimate of the induced gate error, $\epsilon \sim \dot{n}\tau_G$. Typical room-temperature surface-electrode traps show heating rates of $\mathcal{O}(100)\text{Hz}$ [54, 55], for which the induced gate error is roughly $\epsilon \sim 10^{-4}$. As the gate mechanism is completely insensitive to heating events between fast gate operations [28], and performant even for very large motional occupations [Fig. 1(c-d)], we conclude that fast gates are robust against anomalous heating and motional decoherence of the two-ion system.

SDK implementation for ^{133}Ba – ^{138}Ba .— Next, we outline an exemplary implementation scheme for Raman

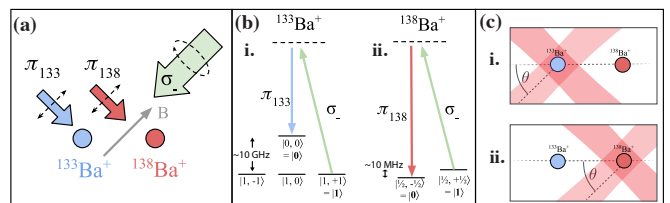


FIG. 2. Implementation of SDKs in a dual-species $^{133}\text{Ba}^+$ – $^{138}\text{Ba}^+$ chain. (a) Configuration of Raman beam orientations, polarizations and magnetic field directions relative to the 2-ion chain. (b) i. Energy levels of the $6s_{1/2}$ manifold in $^{133}\text{Ba}^+$ illustrating the two qubit states and Raman couplings between them. ii. Energy levels and Raman couplings between the qubit states in the $6s_{1/2}$ manifold of $^{138}\text{Ba}^+$. (c) SDKs can be implemented asynchronously, e.g. first an SDK is implemented on $^{133}\text{Ba}^+$ using nanosecond sequences of ultrafast pulses (i.) followed by a single-pulse SDK on $^{138}\text{Ba}^+$ (ii.), as described in the main text.

SDKs in a dual isotopes $^{133}\text{Ba}^+$ – $^{138}\text{Ba}^+$ chain, utilising beams sourced from a single Raman laser, illustrated in Fig. 2(a). The ‘network’ and ‘memory’ qubits are encoded in the $6s_{1/2}$ ground-state manifold of $^{133}\text{Ba}^+$ and $^{138}\text{Ba}^+$, respectively, as shown in Fig. 2(b).

Ultrafast spin-motional entanglement of the $^{133}\text{Ba}^+$ qubit can be realised using a circularly-polarized σ_- beam that illuminates both ions and the linearly-polarized π_{133} beam that solely addresses the $^{133}\text{Ba}^+$ qubit. The large hyperfine splitting of 9.926 GHz in $^{133}\text{Ba}^+$ allows the σ_- and π_{133} beams to resonantly address the $|0,0\rangle \rightarrow |1,+1\rangle$ transition, while minimizing off-resonant couplings to the $|1,-1\rangle$ and $|1,0\rangle$ states (see Fig. 2(b)) and without driving transitions on the $^{138}\text{Ba}^+$ qubit, which has no hyperfine structure. High-fidelity SDKs on the $^{133}\text{Ba}^+$ memory qubit can be realised using nanosecond sequences of ~ 10 pulses sourced from a single ultrafast laser with a repetition rate of several GHz, utilizing pulse sequences developed in Refs. [38, 39].

SDKs on the $^{138}\text{Ba}^+$ network qubit may be performed as demonstrated in [41] using $\mathcal{O}(10)\text{ps}$ pulses of the π_{138} beam instead of π_{133} , in addition to the common σ_- beam. Due to the large frequency separation between the pulse bandwidth ($\sim 10\text{GHz}$) and the Zeeman qubit splitting ($\sim 10\text{MHz}$), SDKs on $^{138}\text{Ba}^+$ can be performed with single pulses, and can be retroreflected with a delay to implement the unitary in Eq. (1) [41]. Furthermore, as the fast gate protocols presented here require only nanosecond control over SDK timings (Fig. 1(e)), SDKs on $^{138}\text{Ba}^+$ can be performed asynchronously to SDKs on the hyperfine qubit without degradation of the two-qubit gate fidelity [see Fig. 2(c)], easing technical constraints for experimental implementation. Alternatively, each resonant π -pulse can be broken into a nanosecond train of weaker pulses to reduce laser power requirements, or even replaced with composite pulse sequences that are

robust to expected noise sources and systematic errors.

Application to photonic interface.— Quantum networks of trapped ions are limited by the rapid dephasing of the Zeeman ‘network’ qubit used to generate ion-photon entanglement, which can be mitigated by rapid transfer of the network qubit into long-lived hyperfine states of an ancillary memory qubit [13, 15]. However, as typical dephasing rates for Zeeman qubits are $\mathcal{O}(1)\text{kHz}$ [3, 5, 14, 15], achieving high-fidelity photonic-mediated entanglement requires fast (MHz speed) coherent transfer of quantum information.

As a concrete example, we consider the implementation of a SWAP operation (consisting of three $\hat{\sigma}_z \otimes \hat{\sigma}_z$ gates, and single-qubit rotations) between a $^{138}\text{Ba}^+$ network and $^{133}\text{Ba}^+$ memory qubit, where the former has a coherence time of 4ms as in the experiment of Ref. [3]. With $\mathcal{N} = 14$ SDKs, $^{133}\text{Ba}^+ - ^{138}\text{Ba}^+$ entangling gates can be performed in approx. 770ns (see Fig. 1(a)), which enables SWAP gate times of approx. $2.4\mu\text{s}$, assuming a 90ns time budget for ultrafast single-qubit operations [38, 39, 56]. The error induced by dephasing of the network qubit can then be estimated as $1 - e^{-2.4\mu\text{s}/(4\text{ms})} \approx 6 \times 10^{-4}$. In comparison, current spectroscopic mixed-species gates have operation times of $\sim 50\mu\text{s}$ [6, 13], which leads to an expected dephasing error of $\approx 4\%$ (assuming a SWAP duration of $150\mu\text{s}$). Even assuming spectroscopic gate times approaching the state-of-the-art for high-fidelity same-species pairs, $\approx 15\mu\text{s}$ [57], the dephasing error would still be $\approx 1\%$ [58].

A secondary limitation of current photonic interconnect schemes is the speed at which remote entanglement can be established, which is currently limited to $\mathcal{O}(100)\text{Hz}$ due to photon collection efficiencies of $\lesssim 10\%$ [5, 43]. This is a technical limitation that may be overcome through the use of integrated optical collection elements, which can feasibly lead to MHz entanglement rates [53, 59]. In this case, local mixed-species operations are expected to become the primary bottleneck in computation speeds [53], further motivating the switch from ‘slow’ (10–100kHz) spectroscopic entangling mechanisms to MHz-speed fast gates – both for mixed-species and same-species local operations on each processing node.

Conclusions.— We have demonstrated the suitability of fast entangling gates based on impulsive SDKs for high-speed and high-fidelity quantum logic gates in a range of mixed-species pairings. Our results indicate that the fast gate mechanism is largely agnostic to the choice of species pair, which enables multiple specialised qubits to be employed on each processing node while retaining the ability to perform high-fidelity and high-speed quantum logic operations between any mixed-species pair. This opens up possibilities for multiple distinct ion species on each QPN for a diverse range of quantum information applications, while retaining the ability to coherently map quantum information and perform log-

ical operations between each pair. Moreover, the adoption of the temperature-insensitive fast gate mechanism is appealing for reducing the rate at which the ions need to be re-cooled, which is a bottleneck in proposed large-scale trapped-ion architectures [60–62].

Acknowledgements.— This research was undertaken with the assistance of supercomputing resources and services from the National Computational Infrastructure, which is supported by the Australian Government.

Appendix A: Gate search details and exemplary solutions

The machine-design of the SDK sequence can be described as the optimisation of Eq. (3) over the SDK directions $\{z_m\}$ and timings $\{t_m\}$. We employ a two-stage procedure, following the GPG scheme developed in Ref. [30]. In the first stage, SDKs are constrained to arrive in N groups with uniformly spaced timings, $t_m = \tau_G m/N$, where τ_G is the desired gate time. For computational simplicity, free evolution between SDKs within each group is neglected in the first stage, such that optimisation is performed over the parameters

$$\vec{z} = \{z_1, z_2, \dots, z_N\}, \quad (\text{A1})$$

where the elements are allowed to take any integer values within a given range. For this work, we use between $N = 16$ and $N = 20$ pulse groups in the first optimisation stage, in order to provide sufficient timing freedoms for high-fidelity solutions, and bound $|z_m| \leq 5$ to limit the number of SDKs in each group. We employ a heuristic approach for optimising the integer parameters z_m : a large ensemble ($10^3 - 10^4$) of randomly sampled initial conditions are propagated by gradient-descent local minimisations, while treating z_m as floating-point numbers. The final solution of each local minimisations are then integerised, and passed onto the second stage of the optimisation.

In the second stage of optimisation, the timings of each SDK group are locally optimised to fine tune the motional trajectories of the ions. In this stage, the finite SDK bandwidth is incorporated by imposing a minimum time separation of 5ns between consecutive pulses in the same group (corresponding to a 200MHz SDK repetition rate). An additional tanh penalty is added to the cost function to prevent temporal overlap of pulse groups. The second stage of optimisation is performed on all candidate solutions identified in the first stage: the optimal SDK sequence is identified as the pulse with the lowest gate error given by Eq. (3). The motional trajectories and SDK sequences for exemplary gate solutions between ^{43}Ca - ^{88}Sr and ^{171}Yb - ^9Be pairs are shown in Fig. A1.

In the gate searches presented in the main text, we assumed the following wavelengths for the Raman lasers used to drive the SDKs on each ion: 532nm for ^{133}Ba and ^{138}Ba [41], 393nm for ^{43}Ca and ^{40}Ca [63, 64], 369.5nm for ^{171}Yb [36, 38, 40, 56], 408nm for ^{88}Sr , and 313nm for ^9Be .

Each gate search requires computation of the secular mode frequencies, which can be solved analytically for a general mixed-species crystal of two ions [65]:

$$\omega_{\text{ip}}^2 = \omega_{0,1}^2 \frac{1 + \mu - \sqrt{1 - \mu + \mu^2}}{\mu}, \quad (\text{A2})$$

$$\omega_{\text{op}}^2 = \omega_{0,1}^2 \frac{1 + \mu + \sqrt{1 - \mu + \mu^2}}{\mu}, \quad (\text{A3})$$

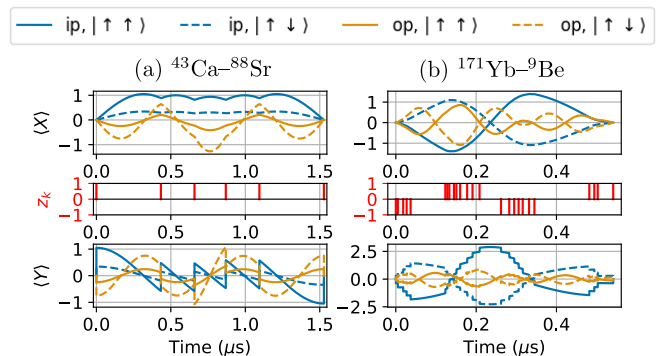


FIG. A1. The motional dynamics of exemplary gate solutions in terms of the pulse sequence z_k , and means of the mode quadratures, $\hat{X} = (\hat{a} + \hat{a}^\dagger)/\sqrt{2}$ and $\hat{Y} = i(\hat{a}^\dagger - \hat{a})/\sqrt{2}$, for the in-phase (ip) and out-of-phase (op) motional modes. (a) illustrates a $1.5\mu\text{s}$ gate between ^{43}Ca and ^{88}Sr using $\mathcal{N} = 6$ SDKs, with intrinsic gate infidelity $\varepsilon_{\text{av}} \approx 2 \times 10^{-10}$. (b) shows a 560ns gate between ^{171}Yb and ^9Be using $\mathcal{N} = 25$ SDKs, with intrinsic gate infidelity $\varepsilon_{\text{av}} \approx 10^{-4}$.

where $\mu = m^{(2)}/m^{(1)}$ is the mass ratio of the mixed-species pair, and $\omega_{0,1}$ is the secular trapping frequency of ion 1 (taken to be 1MHz in the calculations of the main text). The corresponding normal mode eigenvectors for the ip and op modes are given by $\mathbf{b}_{\text{ip}} = (b_1, b_2)$ and $\mathbf{b}_{\text{op}} = (b_1, -b_2)$, respectively, where

$$b_1^2 = \frac{1 - \mu + \sqrt{1 - \mu + \mu^2}}{2\sqrt{1 - \mu + \mu^2}}, \quad (\text{A4})$$

and $b_2 = \sqrt{1 - b_1^2}$.

* zain.mehdi@anu.edu.au

- [1] C. Monroe, R. Raussendorf, A. Ruthven, K. R. Brown, P. Maunz, L.-M. Duan, and J. Kim, Phys. Rev. A **89**, 022317 (2014).
- [2] T. R. Tan, J. P. Gaebler, Y. Lin, Y. Wan, R. Bowler, D. Leibfried, and D. J. Wineland, Nature **528**, 380 (2015).
- [3] I. V. Inlek, C. Crocker, M. Lichtman, K. Sosnova, and C. Monroe, Phys. Rev. Lett. **118**, 250502 (2017).
- [4] C. D. Bruzewicz, R. McConnell, J. Stuart, J. M. Sage, and J. Chiaverini, npj Quantum Inf **5**, 1 (2019).
- [5] L. J. Stephenson, D. P. Nadlinger, B. C. Nichol, S. An, P. Drmota, T. G. Ballance, K. Thirumalai, J. F. Goodwin, D. M. Lucas, and C. J. Ballance, Phys. Rev. Lett. **124**, 110501 (2020).
- [6] A. C. Hughes, V. M. Schäfer, K. Thirumalai, D. P. Nadlinger, S. R. Woodrow, D. M. Lucas, and C. J. Ballance, Phys. Rev. Lett. **125**, 080504 (2020).
- [7] J. P. Home, "Quantum science and metrology with mixed-species ion chains," (2013), arXiv:1306.5950 [physics, physics:quant-ph].
- [8] V. Negnevitsky, M. Marinelli, K. K. Mehta, H.-Y. Lo, C. Flühmann, and J. P. Home, Nature **563**, 527 (2018).

- [9] Y. Wan, D. Kienzler, S. D. Erickson, K. H. Mayer, T. R. Tan, J. J. Wu, H. M. Vasconcelos, S. Glancy, E. Knill, D. J. Wineland, A. C. Wilson, and D. Leibfried, *Science* **364**, 875 (2019).
- [10] F. Lancellotti, S. Welte, M. Simoni, C. Mordini, T. Behrle, B. de Neeve, M. Marinelli, V. Negnevitsky, and J. Home, “Low-excitation transport and separation of high-mass-ratio mixed-species ion chains,” (2023), arXiv:2312.14006 [quant-ph].
- [11] R. Nigmatullin, C. J. Ballance, N. de Beaudrap, and S. C. Benjamin, *New J. Phys.* **18**, 103028 (2016).
- [12] M. Bock, P. Eich, S. Kucera, M. Kreis, A. Lenhard, C. Becher, and J. Eschner, *Nat Commun* **9**, 1998 (2018).
- [13] P. Drmota, D. Main, D. P. Nadlinger, B. C. Nichol, M. A. Weber, E. M. Ainley, A. Agrawal, R. Srinivas, G. Araneda, C. J. Ballance, and D. M. Lucas, *Phys. Rev. Lett.* **130**, 090803 (2023).
- [14] S. Saha, M. Shalaev, J. O’Reilly, I. Goetting, G. Toh, A. Kalakuntla, Y. Yu, and C. Monroe, “High-fidelity remote entanglement of trapped atoms mediated by time-bin photons,” (2024).
- [15] D. Main, P. Drmota, D. P. Nadlinger, E. M. Ainley, A. Agrawal, B. C. Nichol, R. Srinivas, G. Araneda, and D. M. Lucas, “Distributed Quantum Computing across an Optical Network Link,” (2024).
- [16] V. M. Schäfer, C. J. Ballance, K. Thirumalai, L. J. Stephenson, T. G. Ballance, A. M. Steane, and D. M. Lucas, *Nature* **555**, 75 (2018).
- [17] A. Sørensen and K. Mølmer, *Phys. Rev. Lett.* **82**, 1971 (1999).
- [18] J. I. Cirac and P. Zoller, *Phys. Rev. Lett.* **74**, 4091 (1995).
- [19] C. J. Ballance, T. P. Harty, N. M. Linke, M. A. Sepiol, and D. M. Lucas, *Phys. Rev. Lett.* **117**, 060504 (2016).
- [20] C. D. B. Bentley, H. Ball, M. J. Biercuk, A. R. R. Carvalho, M. R. Hush, and H. J. Slatyer, *Adv. Quantum Technol.* **3**, 2000044 (2020).
- [21] P. H. Leung and K. R. Brown, *Phys. Rev. A* **98**, 032318 (2018).
- [22] K. Sosnova, A. Carter, and C. Monroe, *Phys. Rev. A* **103**, 012610 (2021).
- [23] Y. Wu, S.-T. Wang, and L.-M. Duan, *Phys. Rev. A* **97**, 062325 (2018).
- [24] C. Figgatt, A. Ostrander, N. M. Linke, K. A. Landsman, D. Zhu, D. Maslov, and C. Monroe, *Nature* **572**, 368 (2019).
- [25] J. J. García-Ripoll, P. Zoller, and J. I. Cirac, *Phys. Rev. Lett.* **91**, 157901 (2003).
- [26] J. J. García-Ripoll, P. Zoller, and J. I. Cirac, *Phys. Rev. A* **71**, 062309 (2005).
- [27] C. D. B. Bentley, A. R. R. Carvalho, D. Kielpinski, and J. J. Hope, *New J. Phys.* **15**, 043006 (2013).
- [28] R. L. Taylor, C. D. B. Bentley, J. S. Pedernales, L. Lamata, E. Solano, A. R. R. Carvalho, and J. Hope, *Scientific Reports* **7**, 46197 (2017), 1601.00359.
- [29] A. Ratcliffe, R. Taylor, J. Hope, and A. Carvalho, *Phys. Rev. Lett.* **120**, 220501 (2018).
- [30] E. P. G. Gale, Z. Mehdi, L. M. Oberg, A. K. Ratcliffe, S. A. Haine, and J. J. Hope, *Phys. Rev. A* **101**, 052328 (2020).
- [31] A. Ratcliffe, L. Oberg, and J. Hope, *Phys. Rev. A* **101**, 052332 (2020).
- [32] Z. Mehdi, A. K. Ratcliffe, and J. J. Hope, *Phys. Rev. Research* **3**, 013026 (2021).
- [33] Z. Mehdi, A. K. Ratcliffe, and J. Hope, *Phys. Rev. A* **102**, 012618 (2020).
- [34] E. Torrontegui, D. Heinrich, M. I. Hussain, R. Blatt, and J. J. García-Ripoll, *New Journal of Physics* **22**, 103024 (2020).
- [35] Y.-K. Wu and L.-M. Duan, *Chinese Phys. Lett.* **37**, 070302 (2020).
- [36] J. D. Wong-Campos, S. A. Moses, K. G. Johnson, and C. Monroe, *Phys. Rev. Lett.* **119**, 230501 (2017).
- [37] See Supplemental Material at [url], which includes a detailed derivation of Eqs. (1-3), and additional error analysis.
- [38] J. Mizrahi, C. Senko, B. Neyenhuis, K. G. Johnson, W. C. Campbell, C. W. S. Conover, and C. Monroe, *Phys. Rev. Lett.* **110**, 203001 (2013), arXiv:1201.6597 [physics, physics:quant-ph].
- [39] J. Mizrahi, B. Neyenhuis, K. G. Johnson, W. C. Campbell, C. Senko, D. Hayes, and C. Monroe, *Applied Physics B* **114**, 45–61 (2013).
- [40] W.-X. Guo, Y.-K. Wu, Y.-Y. Huang, L. Feng, C.-X. Huang, H.-X. Yang, J.-Y. Ma, L. Yao, Z.-C. Zhou, and L.-M. Duan, *Phys. Rev. A* **106**, 022608 (2022).
- [41] R. Putnam, A. D. West, W. C. Campbell, and P. Hamilton, *Phys. Rev. A* **109**, 032614 (2024).
- [42] C. Aughter, C.-K. Chou, T. W. Noel, and B. B. Blinov, *Journal of the Optical Society of America B* **31**, 1568 (2014).
- [43] J. O’Reilly, G. Toh, I. Goetting, S. Saha, M. Shalaev, A. L. Carter, A. Risinger, A. Kalakuntla, T. Li, A. Verma, and C. Monroe, *Phys. Rev. Lett.* **133**, 090802 (2024).
- [44] C. D. Bruzewicz, R. McConnell, J. Stuart, J. M. Sage, and J. Chiaverini, *npj Quantum Inf* **5**, 1 (2019).
- [45] C. J. Ballance, V. M. Schäfer, J. P. Home, D. J. Szwer, S. C. Webster, D. T. C. Allcock, N. M. Linke, T. P. Harty, D. P. L. Aude Craik, D. N. Stacey, A. M. Steane, and D. M. Lucas, *Nature* **528**, 384 (2015).
- [46] V. M. Schäfer, *Fast Gates and Mixed-Species Entanglement with Trapped Ions*, Springer Theses (Springer International Publishing, Cham, 2020).
- [47] T. Clark, T. Carruthers, P. Matthews, and I. Duling, *Electronics Letters* **35**, 720–721 (1999).
- [48] S. Charles Doret, J. M. Amini, K. Wright, C. Volin, T. Killian, A. Ozakin, D. Denison, H. Hayden, C.-S. Pai, R. E. Slusher, and A. W. Harter, *New Journal of Physics* **14**, 073012 (2012).
- [49] Z Mehdi, A. K. Ratcliffe, and J. Hope, *Phys. Rev. Res.* **3**, 013026 (2021).
- [50] K. G. Johnson, J. D. Wong-Campos, B. Neyenhuis, J. Mizrahi, and C. Monroe, *Nature Communications* **8** (2017), 10.1038/s41467-017-00682-6.
- [51] K. Johnson, B. Neyenhuis, J. Mizrahi, J. Wong-Campos, and C. Monroe, *Physical Review Letters* **115** (2015), 10.1103/physrevlett.115.213001.
- [52] A. G. Fowler, M. Mariantoni, J. M. Martinis, and A. N. Cleland, *Phys. Rev. A* **86**, 032324 (2012).
- [53] N. H. Nickerson, J. F. Fitzsimons, and S. C. Benjamin, *Phys. Rev. X* **4**, 041041 (2014).
- [54] T. P. Harty, D. T. C. Allcock, C. J. Ballance, L. Guidoni, H. A. Janacek, N. M. Linke, D. N. Stacey, and D. M. Lucas, *Phys. Rev. Lett.* **113**, 220501 (2014).
- [55] C. D. Bruzewicz, J. M. Sage, and J. Chiaverini, *Phys. Rev. A* **91**, 041402 (2015).
- [56] W. C. Campbell, J. Mizrahi, Q. Quraishi, C. Senko, D. Hayes, D. Hucul, D. N. Matsukevich, P. Maunz, and

- C. Monroe, Phys. Rev. Lett. **105**, 090502 (2010).
- [57] S. Saner, O. Băzăvan, M. Minder, P. Drmota, D. J. Webb, G. Araneda, R. Srinivas, D. M. Lucas, and C. J. Ballance, Phys. Rev. Lett. **131**, 220601 (2023).
- [58] These estimates are consistent with $\mathcal{O}(1\%)$ dephasing error contributions to remote entanglement fidelities observed in experiment [5, 15].
- [59] F. W. Knollmann, E. Clements, P. T. Callahan, M. Gehl, J. D. Hunker, T. Mahony, R. McConnell, R. Swint, C. Sorace-Agaskar, I. L. Chuang, J. Chiaverini, and D. Stick, “Integrated photonic structures for photon-mediated entanglement of trapped ions,” (2024).
- [60] J. M. Pino, J. M. Dreiling, C. Figgatt, J. P. Gaebler, S. A. Moses, M. S. Allman, C. H. Baldwin, M. Foss-Feig, D. Hayes, K. Mayer, C. Ryan-Anderson, and B. Neyenhuis, Nature **592**, 209 (2021).
- [61] M. Cetina, L. Egan, C. Noel, M. Goldman, D. Biswas, A. Risinger, D. Zhu, and C. Monroe, PRX Quantum **3**, 010334 (2022).
- [62] S. A. Moses, C. H. Baldwin, M. S. Allman, R. Ancona, L. Ascarrunz, C. Barnes, J. Bartolotta, B. Bjork, P. Blanchard, M. Bohn, J. G. Bohnet, N. C. Brown, N. Q. Burdick, W. C. Burton, S. L. Campbell, J. P. Campora, C. Carron, J. Chambers, J. W. Chan, Y. H. Chen, A. Chernoguzov, E. Chertkov, J. Colina, J. P. Curtis, R. Daniel, M. DeCross, D. Deen, C. Delaney, J. M. Dreiling, C. T. Ertsgaard, J. Esposito, B. Estey, M. Fabrikant, C. Figgatt, C. Foltz, M. Foss-Feig, D. Francois, J. P. Gaebler, T. M. Gatterman, C. N. Gilbreth, J. Giles, E. Glynn, A. Hall, A. M. Hankin, A. Hansen, D. Hayes, B. Higashi, I. M. Hoffman, B. Horning, J. J. Hout, R. Jacobs, J. Johansen, L. Jones, J. Karcz, T. Klein, P. Lauria, P. Lee, D. Liefer, S. T. Lu, D. Lucchetti, C. Lytle, A. Malm, M. Matheny, B. Mathewson, K. Mayer, D. B. Miller, M. Mills, B. Neyenhuis, L. Nugent, S. Olson, J. Parks, G. N. Price, Z. Price, M. Pugh, A. Ransford, A. P. Reed, C. Roman, M. Rowe, C. Ryan-Anderson, S. Sanders, J. Sedlacek, P. Shevchuk, P. Siegfried, T. Skripka, B. Spaun, R. T. Sprenkle, R. P. Stutz, M. Swallows, R. I. Tobey, A. Tran, T. Tran, E. Vogt, C. Volin, J. Walker, A. M. Zolot, and J. M. Pino, Phys. Rev. X **13**, 041052 (2023).
- [63] M. I. Hussain, M. Guevara-Bertsch, E. Torrontegui, J. J. Garcia-Ripoll, R. Blatt, and C. F. Roos, “Single-ion optical autocorrelator,” (2023), arXiv:2312.03679 [quant-ph].
- [64] D. Heinrich, M. Guggemos, M. Guevara-Bertsch, M. I. Hussain, C. F. Roos, and R. Blatt, New J. Phys. **21**, 073017 (2019).
- [65] J. B. Wübbena, S. Amairi, O. Mandel, and P. O. Schmidt, Physical Review A **85** (2012), 10.1103/physreva.85.043412.
- [66] This assumption is not required for the two-qubit entangling gate mechanism, as otherwise the phase of the SDK would be proportional to the relative phase between the counter-propagating pair, which can be characterised and thus eliminated with single-qubit rotations.
- [67] C. Bentley, A. Carvalho, D. Kielpinski, and J. Hope, New Journal of Physics **15**, 043006 (2013), arXiv:1211.7156 [quant-ph].

Supplemental Materials for ‘Fast mixed-species quantum logic gates for trapped-ion quantum networks’

In this supplemental material we provide (1) a detailed derivation of the unitary operator and condition equations for the fast entangling gate mechanism (Eqs. (1-2) of the main text), (2) a detailed derivation of the state-averaged infidelity (Eq. (3) of the main text), and (3) additional error analysis of the fast gate mechanism under timing jitter and frequency shifts.

(1) Gate unitary and phase gate condition equations

Here we provided a detailed derivation of the unitary operator describing a heterogeneous fast gate protocol composed of \mathcal{N} state-dependent kicks (SDKs) interspersed by free motional evolution, which generalises previous derivations for same-species systems [25, 26].

State-dependent kicks

An SDK can be realised using a pair of counter-propagating π -pulses. Each π -pulse performs a population inversion of the qubit state, alongside a photon recoil of $\pm\hbar k$: the unitary operator for a π -pulse incident on the j -th ion is described by the unitary operator:

$$U_{\pi}^{(j)}(k^{(j)}) = \sigma_{-} e^{i(k^{(j)}\hat{x}^{(j)} + \phi_L)} + h.c. = \sigma_x^{(j)} e^{i(k^{(j)}\hat{x}^{(j)} + \phi_L)\sigma_z^{(j)}}, \quad (S1)$$

where ϕ_L is the laser phase. The counter-propagating π -pulse is described by the same unitary, with inverted wavevector $k^{(j)} \rightarrow -k^{(j)}$. We additionally assume the counter-propagating pulse to carry phase $-\phi_L$, such that the contribution of the laser phase cancels for each SDK [66]. Assuming the time delay between the two pulses is much faster

than the motion of the ions, an SDK incident on each of the two target ions can be written as:

$$U_{\text{SDK}} \equiv U_{\pi}^{(2)}(-k^{(2)})U_{\pi}^{(1)}(-k^{(1)})U_{\pi}^{(2)}(k^{(2)})U_{\pi}^{(1)}(k^{(1)}) = e^{2i(k^{(1)}\hat{x}^{(1)}\sigma_z^{(1)}+k^{(2)}\hat{x}^{(2)}\sigma_z^{(2)})}. \quad (\text{S2})$$

We then proceed by expanding the position operator of each ion in terms of quantized normal modes:

$$\hat{x}^{(j)} = \sum_{\alpha} b_{\alpha}^{(j)} \sqrt{\frac{\hbar}{m^{(j)}\omega_{\alpha}}} \hat{X}_{\alpha}, \quad (\text{S3})$$

where $m^{(j)}$ is the mass of the j -th ion, $b_{\alpha}^{(j)}$ gives the coupling of the j -th ion to the α -th normal mode, and we have defined the dimensionless position quadrature of the α -th motional mode, $\hat{X}_{\alpha} \equiv (\hat{a}_{\alpha} + \hat{a}_{\alpha}^{\dagger})/\sqrt{2}$. Using Eq. (S3), the SDK unitary can be written as a product of displacement operators on each motional mode, $\hat{D}_{\alpha}(\beta) = \exp\{\beta\hat{a}_{\alpha}^{\dagger} - \beta^*\hat{a}_{\alpha}\}$, i.e.

$$U_{\text{SDK}}(k^{(1)}, k^{(2)}) = \prod_{j=1,2} \prod_{\alpha} \hat{D}_{\alpha} \left(2ib_{\alpha}^{(j)}\eta_{\alpha}^{(j)}\hat{\sigma}_z^{(j)} \right), \quad (\text{S4})$$

where $\eta_{\alpha}^{(j)} = k^{(j)}\sqrt{\hbar/(2m^{(j)}\omega_{\alpha})}$ is the mode- and ion-dependent Lamb-Dicke parameter.

It is then straightforward to describe the action of a single SDK on a general two-qubit state of the form:

$$|\psi_0\rangle = (c_{\uparrow\uparrow}|\uparrow\uparrow\rangle + c_{\uparrow\downarrow}|\uparrow\downarrow\rangle + c_{\downarrow\uparrow}|\downarrow\uparrow\rangle + c_{\downarrow\downarrow}|\downarrow\downarrow\rangle) \otimes |\psi_{\text{mot}}\rangle, \quad (\text{S5})$$

where we have assumed a pure motional state, $|\psi_{\text{mot}}\rangle$, shared by all internal states. For the present study, where all operations are either displacements or rotations in phase, it is sufficient to consider the case where the motional state is a product of coherent states of each motional mode, i.e. $|\psi_{\text{mot}}\rangle = \otimes_{\alpha} |\beta_{\alpha,0}\rangle$, where $\beta_{\alpha,0}$ is the initial coherent state amplitude of the α -th motional mode. In this case, the kicked state $|\psi_{\text{kicked}}\rangle = \hat{U}_{\text{SDK}}|\psi_0\rangle$ becomes:

$$|\psi_{\text{kicked}}\rangle = \bigotimes_{\alpha} \left[(c_{\uparrow\uparrow}|\uparrow\uparrow\rangle |\beta_{\alpha,0} + 4i\bar{\eta}_{\alpha}^{+}\rangle + c_{\downarrow\downarrow}|\downarrow\downarrow\rangle |\beta_{\alpha,0} - 4i\bar{\eta}_{\alpha}^{+}\rangle) \right. \\ \left. + (c_{\uparrow\downarrow}|\uparrow\downarrow\rangle |\beta_{\alpha,0} - 4i\bar{\eta}_{\alpha}^{-}\rangle + c_{\downarrow\uparrow}|\downarrow\uparrow\rangle |\beta_{\alpha,0} + 4i\bar{\eta}_{\alpha}^{-}\rangle) \right], \quad (\text{S6})$$

where we defined the effective Lamb-Dicke couplings to the centre-of-mass (+) and relative (-) coordinates:

$$\bar{\eta}_{\alpha}^{+} = \frac{1}{2} \left(b_{\alpha}^{(1)}\eta_{\alpha}^{(1)} + b_{\alpha}^{(2)}\eta_{\alpha}^{(2)} \right), \quad (\text{S7a})$$

$$\bar{\eta}_{\alpha}^{-} = \frac{1}{2} \left(b_{\alpha}^{(2)}\eta_{\alpha}^{(2)} - b_{\alpha}^{(1)}\eta_{\alpha}^{(1)} \right). \quad (\text{S7b})$$

These parameters describe the effective coupling of the SDK to the same-spin two-qubit states (CM: $\{|\uparrow\uparrow\rangle, |\downarrow\downarrow\rangle\}$) and opposite spin-states (rel: $\{|\uparrow\downarrow\rangle, |\downarrow\uparrow\rangle\}$), respectively.

Derivation of Eq. (2) of the main text

As derived in the main text, the unitary for the pulsed fast gate operation is given by a product of impulsive SDKs at times t_m with wavevector z_mk (where $z_m = \pm 1$ denotes the pulse direction), interspersed by free motional evolution:

$$\hat{U}_{\text{G}} = \prod_{m=1}^{\mathcal{N}} \hat{U}_{\text{free}}(t_{m+1} - t_m) \hat{U}_{\text{SDK}}(z_mk_1, z_mk_2), \quad (\text{S8})$$

where $U_{\text{free}}(t) = \prod_{\alpha} \exp\{-i\omega_{\alpha}(\hat{a}_{\alpha}^{\dagger}\hat{a}_{\alpha} + 1/2)t\}$ describes free harmonic evolution of each motional mode with (secular) mode frequency ω_{α} . The duration of the gate operation is set by the time between the first and last SDK; in ideal operation, the final free evolution period has no effect on the two-qubit entanglement, nor does free evolution prior to the first pulse. Therefore, we can equivalently express the gate unitary as:

$$\hat{U}_{\text{G}} = \prod_{m=1}^{\mathcal{N}} \hat{U}_{\text{SDK}}(z_mk_1, z_mk_2) \hat{U}_{\text{free}}(\delta t_m), \quad (\text{S9})$$

where $\delta t_m = t_m - t_{m-1}$, and we can set $\delta t_1 = 0$ without loss of generality.

Noting that the SDK unitary, Eq. (S4), leaves the two-qubit state unchanged, the gate unitary must be diagonal in the two-qubit basis $\{|\uparrow\uparrow\rangle, |\uparrow\downarrow\rangle, |\downarrow\uparrow\rangle, |\downarrow\downarrow\rangle\}$. Thus, it is sufficient to consider the action of \hat{U}_G on each two-qubit state independently.

Consider the action of the gate unitary on the same-spin state $|\uparrow\uparrow\rangle$. Assuming an the initial state given by Eq. (S5), the final motional state associated with this two-qubit state is given by a product of coherent states for each mode

$$\langle\uparrow\uparrow|\hat{U}_G|\psi_0\rangle = \prod_m \prod_\alpha \hat{D}_\alpha(4iz_m\bar{\eta}_\alpha^+) e^{-i\omega_\alpha \hat{a}_\alpha^\dagger \hat{a}_\alpha \delta t_m} \left[\bigotimes_\alpha |\beta_{\alpha,0}\rangle \right], \quad (\text{S10})$$

where $\delta t_m = t_{m+1} - t_m$. We may then consider each motional mode independently to derive a relation between $\beta_\alpha^{\uparrow\uparrow}(\tau_G)$ and $\beta_{\alpha,0}$, where $\tau_G = \sum_m t_m$ is the gate operation time. We use several properties of displacement and rotation operations on coherent states – $|\beta\rangle = \hat{D}(\beta)|0\rangle$ (where $|0\rangle$ is the vacuum, and we have dropped mode-dependent subscripts), $e^{-i\Theta\hat{a}^\dagger\hat{a}}|\beta\rangle = |\beta e^{-i\Theta}\rangle$, and $\hat{D}(a)\hat{D}(b) = e^{i\text{Im}[ab^*]}\hat{D}(a+b)$ – in the calculation that follows. First, we relate the motional state after k iterations to the motional state after $k-1$ iterations, $|\beta_{\alpha,k-1}\rangle$, i.e.

$$\hat{D}_\alpha(4iz_k\bar{\eta}_\alpha^+) e^{-i\omega_\alpha \hat{a}_\alpha^\dagger \hat{a}_\alpha \delta t_k} |\beta_{\alpha,k-1}\rangle = e^{i\text{Im}\{4iz_k\bar{\eta}_\alpha^+ \beta_{\alpha,k-1}^*\}} |e^{-i\omega_\alpha \delta t_k} \beta_{\alpha,k-1} + 4iz_k\bar{\eta}_\alpha^+\rangle. \quad (\text{S11})$$

Then, to identify the final state after \mathcal{N} SDKs, we need to figure out the complex amplitude of the final coherent state, as well as the accumulated phase due to displacements generated by non-commuting operators.

First, we find the final coherent state amplitude. From Eq. (S11), we can identify the following recursion relation for the amplitude of each mode:

$$\beta_{\alpha,k} = e^{-i\omega_\alpha \delta t_k} \beta_{\alpha,k-1} + 4iz_k\bar{\eta}_\alpha^+, \quad (\text{S12})$$

$$= 4i\bar{\eta}_\alpha^+ \sum_{n=1}^k z_n e^{-i\omega_\alpha \sum_{j=n}^k \delta t_j} + \beta_{\alpha,0} e^{-i\omega_\alpha t_k}, \quad (\text{S13})$$

where we have obtained the second line by expanding out the recursion relation in terms of the initial coherent state amplitude, $\beta_{\alpha,0}$. The second term describes free evolution of the motional mode if there were no SDKs – as $\beta_{\alpha,0} = 0$ can be taken without loss of generality, the first term thus describes the effect of the kicks. Then, noting $\sum_{j=n}^k \delta t_j = t_k - t_n$, we can identify the final coherent state amplitude:

$$\beta_{\alpha,\mathcal{N}} = \left(4i\bar{\eta}_\alpha^+ \sum_{n=1}^{\mathcal{N}} z_n e^{i\omega_\alpha t_n} + \beta_{\alpha,0} \right) e^{-i\omega_\alpha \tau_G}, \quad (\text{S14})$$

where $\tau_G = \sum_n t_n$ is the gate operation time. Moving into the rotating frame of each of the motional modes, the final coherent state amplitude can then be written as:

$$\beta_{\alpha,\mathcal{N}}^{(\text{rot.})} = 4i\bar{\eta}_\alpha^+ \sum_{n=1}^{\mathcal{N}} z_n e^{i\omega_\alpha t_n} + \beta_{\alpha,0}. \quad (\text{S15})$$

A similar calculation yields the final motional amplitudes for the other two-qubit states:

$$\beta_{\alpha,\mathcal{N}}^{\downarrow\downarrow} = -\beta_{\alpha,\mathcal{N}}^{\uparrow\uparrow}, \quad (\text{S16})$$

$$\beta_{\alpha,\mathcal{N}}^{\downarrow\uparrow} = 4i\bar{\eta}_\alpha^- \sum_{n=1}^{\mathcal{N}} z_n e^{i\omega_\alpha t_n} + \beta_{\alpha,0}, \quad (\text{S17})$$

$$\beta_{\alpha,\mathcal{N}}^{\uparrow\downarrow} = -\beta_{\alpha,\mathcal{N}}^{\downarrow\uparrow}. \quad (\text{S18})$$

Henceforth we will adopt the shorthand notation $\beta_\alpha^+ \equiv \beta_{\alpha,\mathcal{N}}^{\uparrow\uparrow} = -\beta_{\alpha,\mathcal{N}}^{\downarrow\downarrow}$ and $\beta_\alpha^- \equiv \beta_{\alpha,\mathcal{N}}^{\downarrow\uparrow} = -\beta_{\alpha,\mathcal{N}}^{\uparrow\downarrow}$.

In order for the internal qubit states and motional degrees of freedom to decouple by the end of the gate operation, the final coherent state amplitude should be the same as if there were no SDKs and only free evolution for period τ_G [25]. By inspection of the above equations, this implies the motional restoration condition:

$$\sum_{n=1}^{\mathcal{N}} z_n e^{i\omega_\alpha t_n} = 0, \quad \forall \alpha. \quad (\text{S19})$$

Next, we consider the phase accumulated by the $|\uparrow\uparrow\rangle$ two-qubit state during the gate operation. By inspection of Equation (S10), we can identify the two-qubit phase arising from the non-commutativity of displacement operators along non-commuting axes in phase space (see Eq. (S11)):

$$\Theta_{\alpha}^{\uparrow\uparrow} = 4\bar{\eta}_{\alpha}^{+} \sum_{m=1}^{\mathcal{N}} z_m \operatorname{Im}\{i\beta_{\alpha,k-1}^{*} e^{i\omega_{\alpha}\delta t_m}\}, \quad (\text{S20})$$

which is a mode-dependent quantity. Using the recursion relation for the coherent state amplitude, Eq. (S14), the latter expression may be written as:

$$\Theta_{\alpha}^{\uparrow\uparrow} = 4\bar{\eta}_{\alpha}^{+} \sum_{k=1}^{\mathcal{N}} z_k \left(4\bar{\eta}_{\alpha}^{+} \sum_{n=1}^{k-1} z_n \sin(\omega_{\alpha}[t_k - t_n]) + \operatorname{Re}[\beta_{\alpha,0}^{*} e^{i\omega_{\alpha}t_k}] \right) \quad (\text{S21})$$

$$= 16(\bar{\eta}_{\alpha}^{+})^2 \sum_{m=2}^{\mathcal{N}} \sum_{n=1}^{m-1} z_n z_m \sin(\omega_{\alpha}[t_m - t_n]) + 8\bar{\eta}_{\alpha}^{+} \sum_{k=1}^{\mathcal{N}} z_k \operatorname{Re}[\beta_{\alpha,0}^{*} e^{i\omega_{\alpha}t_k}]. \quad (\text{S22})$$

Without loss of generality, we may choose the initial coherent state amplitude to be $\beta_{\alpha,0} = 0$, in which case the latter term in the above expression vanishes. The total phase accumulated by the $|\uparrow\uparrow\rangle$ state is then given by summing over all motional modes:

$$\Theta^{\uparrow\uparrow} = 16 \sum_{\alpha} (\bar{\eta}_{\alpha}^{+})^2 \sum_{m=2}^{\mathcal{N}} \sum_{n=1}^{m-1} z_n z_m \sin(\omega_{\alpha}[t_m - t_n]). \quad (\text{S23})$$

An analogous calculation for the other two-qubit basis states yields the phases accumulated by each,

$$\Theta^{\downarrow\downarrow} = \Theta^{\uparrow\uparrow}, \quad (\text{S24a})$$

$$\Theta^{\downarrow\uparrow} = 16 \sum_{\alpha} (\bar{\eta}_{\alpha}^{-})^2 \sum_{m=2}^{\mathcal{N}} \sum_{n=1}^{m-1} z_n z_m \sin(\omega_{\alpha}[t_m - t_n]), \quad (\text{S24b})$$

$$\Theta^{\uparrow\downarrow} = \Theta^{\downarrow\uparrow}. \quad (\text{S24c})$$

Then, assuming that the motional restoration condition, Eq. (S19), is satisfied, we may express the unitary for the gate in the two-qubit basis as the matrix:

$$\hat{U}_{\text{G}} = \begin{pmatrix} \exp(i\Theta^{\uparrow\uparrow}) & 0 & 0 & 0 \\ 0 & \exp(i\Theta^{\downarrow\uparrow}) & 0 & 0 \\ 0 & 0 & \exp(i\Theta^{\uparrow\downarrow}) & 0 \\ 0 & 0 & 0 & \exp(i\Theta^{\downarrow\downarrow}) \end{pmatrix} = \exp\left(i\frac{\Theta^{\uparrow\uparrow} + \Theta^{\downarrow\uparrow}}{2}\right) \exp\left\{i\Theta\hat{\sigma}_z^{(1)} \otimes \hat{\sigma}_z^{(2)}\right\}, \quad (\text{S25})$$

which is, up to a global phase, a $\sigma_z \otimes \sigma_z$ phase gate with relative phase Θ given by:

$$\Theta \equiv \frac{\Theta^{\uparrow\uparrow} - \Theta^{\downarrow\uparrow}}{2} = 8 \sum_{\alpha} [(\bar{\eta}_{\alpha}^{+})^2 - (\bar{\eta}_{\alpha}^{-})^2] \sum_{m=2}^{\mathcal{N}} \sum_{n=1}^{m-1} z_n z_m \sin(\omega_{\alpha}[t_m - t_n]), \quad (\text{S26})$$

$$= 8 \sum_{\alpha} b_{\alpha}^{(1)} b_{\alpha}^{(2)} \eta_{\alpha}^{(1)} \eta_{\alpha}^{(2)} \sum_{m=2}^{\mathcal{N}} \sum_{n=1}^{m-1} z_n z_m \sin(\omega_{\alpha}[t_m - t_n]). \quad (\text{S27})$$

We have substituted Eq. (S7) to obtain the second line, and this expression is Eq. (2) of the main text. It is straightforward to check that eliminating the ion dependence of the Lamb-Dicke parameter in the above expression, i.e. setting $\eta_{\alpha}^{(1)} = \eta_{\alpha}^{(2)} \equiv \eta_{\alpha}$, recovers the same-species result [25–27, 29, 30, 67]:

$$\Theta = 8 \sum_{\alpha} b_{\alpha}^{(1)} b_{\alpha}^{(2)} \eta_{\alpha}^2 \sum_{m=2}^{\mathcal{N}} \sum_{n=1}^{m-1} z_n z_m \sin(\omega_{\alpha}[t_m - t_n]). \quad (\text{S28})$$

(2) Fidelity derivation

Ideally, fast gates implement a maximally-entangling $\sigma_z \otimes \sigma_z$ phase gate, described by the unitary operator

$$\hat{U}_{\text{id}} = e^{i(\pi/4)\sigma_z^{(1)}\sigma_z^{(2)}} = \begin{pmatrix} e^{i\pi/4} & 0 & 0 & 0 \\ 0 & e^{-i\pi/4} & 0 & 0 \\ 0 & 0 & e^{-i\pi/4} & 0 \\ 0 & 0 & 0 & e^{i\pi/4} \end{pmatrix}, \quad (\text{S29})$$

up to a global phase. For a given two-qubit state, $|\psi_0\rangle$, the fidelity of a fast gate is given by

$$\mathcal{F}_{|\psi_0\rangle} = \text{Tr}_m \left[\langle \psi_0 | \hat{U}_{\text{id}}^\dagger \hat{U}_{\text{gate}} |\psi_0\rangle \langle \psi_0 | \otimes \hat{\rho}_m \hat{U}_{\text{gate}}^\dagger \hat{U}_{\text{id}} |\psi_0\rangle \right], \quad (\text{S30})$$

where the trace is over the motional degrees of freedom with initial state $\hat{\rho}_m$, and the unitary operator describing the fast gate operation is given by:

$$\hat{U}_{\text{gate}} = \begin{pmatrix} e^{i\Theta^{\uparrow\uparrow}} \hat{D}_{\downarrow\downarrow} & 0 & 0 & 0 \\ 0 & e^{i\Theta^{\uparrow\downarrow}} \hat{D}_{\downarrow\uparrow} & 0 & 0 \\ 0 & 0 & e^{i\Theta^{\downarrow\downarrow}} \hat{D}_{\uparrow\downarrow} & 0 \\ 0 & 0 & 0 & e^{i\Theta^{\downarrow\uparrow}} \hat{D}_{\uparrow\uparrow} \end{pmatrix}, \quad (\text{S31})$$

where

$$\Theta^{\uparrow\uparrow/\downarrow\uparrow} = 16 \sum_{\alpha} (\bar{\eta}_{\alpha}^{\pm})^2 \sum_{m=2}^{\mathcal{N}} \sum_{n=1}^{m-1} z_n z_m \sin(\omega_{\alpha}[t_m - t_n]). \quad (\text{S32})$$

Then, moving into the rotating frame of each motional mode, we can describe the residual motion at the end of the gate by the displacement operators (noting that displacement operators for different modes commute):

$$\hat{D}_{\downarrow\downarrow} = (\hat{D}_{\uparrow\uparrow})^\dagger = \prod_{\alpha} \hat{D}_{\alpha}(-\beta_{\alpha}^+), \quad (\text{S33a})$$

$$\hat{D}_{\downarrow\uparrow} = (\hat{D}_{\uparrow\downarrow})^\dagger = \prod_{\alpha} \hat{D}_{\alpha}(-\beta_{\alpha}^-), \quad (\text{S33b})$$

where we have defined the displacement amplitudes:

$$\beta_{\alpha}^{\pm} = 4i\bar{\eta}^{\pm} \sum_k z_k e^{i\omega_{\alpha} t_k}. \quad (\text{S34})$$

Then, using the cyclic nature of the trace, Eq. (S30) can be written as:

$$\mathcal{F}_{|\psi_0\rangle} = \text{Tr}_m \left[\hat{A}^\dagger \hat{A} \hat{\rho}_m \right] \equiv \langle \hat{A}^\dagger \hat{A} \rangle_m, \quad (\text{S35})$$

where

$$\hat{A} = \langle \psi_0 | \hat{U}_{\text{id}}^\dagger \hat{U}_{\text{gate}} |\psi_0\rangle = e^{i(-\pi/4)} \left(P_{\downarrow\downarrow} \hat{D}_{\downarrow\downarrow} + P_{\uparrow\uparrow} \hat{D}_{\uparrow\uparrow} \right) + e^{i(\Theta^{\downarrow\uparrow} + \pi/4)} \left(P_{\downarrow\uparrow} \hat{D}_{\downarrow\uparrow} + P_{\uparrow\downarrow} \hat{D}_{\uparrow\downarrow} \right), \quad (\text{S36})$$

and P_{ij} is the probability of the two-qubit state $|ij\rangle$, satisfying the normalisation condition:

$$\sum_{i,j=\uparrow,\downarrow} P_{ij} = 1. \quad (\text{S37})$$

Note that the fidelity is independent of the relative phases of the two-qubit states; this is an artefact assuming perfect π -pulses, such that each SDK exactly restores the internal state of the ions. The expression for the fidelity will then

become a linear combination of pairs of displacement operators, which can be simplified using the fact that motional operators on different modes commute to compute products of displacement operators, e.g.

$$\hat{D}_{\downarrow\downarrow}\hat{D}_{\uparrow\uparrow} = \prod_{\alpha} \hat{D}_{\alpha}(-\beta_{\alpha}^{+})\hat{D}_{\alpha}(-\beta_{\alpha}^{-}), \quad (\text{S38})$$

$$= \prod_{\alpha} \hat{D}_{\alpha}(-(\beta_{\alpha}^{+} + \beta_{\alpha}^{-})), \quad (\text{S39})$$

$$= \prod_{\alpha} \hat{D}_{\alpha}(-4i\bar{\eta}^{(2)} \sum_k z_k e^{i\omega_{\alpha}t_k}) \equiv \prod_{\alpha} \hat{D}_{\alpha}(-\beta_{\alpha}^{(2)}). \quad (\text{S40})$$

Here we have used the relation $\hat{D}(\alpha)\hat{D}(\beta) = e^{\alpha\beta^{*}-\alpha^{*}\beta}\hat{D}(\alpha+\beta)$ to obtain the second line – noting β_{α}^{+} and β_{α}^{-} share the same complex phase – and substituted $\bar{\eta}_{\alpha}^{\pm} = (\bar{\eta}^{(2)} \pm \bar{\eta}^{(1)})/2$ to obtain the final line. Similarly, other pairs of displacement operators can be simplified:

$$\hat{D}_{\uparrow\uparrow}\hat{D}_{\uparrow\downarrow} = \left(\hat{D}_{\downarrow\downarrow}\hat{D}_{\downarrow\uparrow}\right)^{\dagger} = \prod_{\alpha} \hat{D}_{\alpha}(\beta_{\alpha}^{(2)}), \quad (\text{S41})$$

$$\hat{D}_{\uparrow\uparrow}\hat{D}_{\downarrow\uparrow} = \prod_{\alpha} \hat{D}_{\alpha}(\beta_{\alpha}^{(1)}), \quad (\text{S42})$$

$$\hat{D}_{\downarrow\downarrow}\hat{D}_{\uparrow\downarrow} = \left(\hat{D}_{\uparrow\uparrow}\hat{D}_{\downarrow\uparrow}\right)^{\dagger} = \prod_{\alpha} \hat{D}_{\alpha}(-\beta_{\alpha}^{(1)}). \quad (\text{S43})$$

Using the above result, the fidelity expression becomes:

$$\begin{aligned} \mathcal{F}_{|\psi_0\rangle} &= \underbrace{P_{\uparrow\uparrow}^2 + P_{\uparrow\downarrow}^2 + P_{\downarrow\uparrow}^2 + P_{\downarrow\downarrow}^2}_{=1} \\ &= -ie^{-i\Theta^{\uparrow\uparrow}} \left\langle P_{\uparrow\uparrow} \left(\hat{D}_{\alpha}(\beta_{\alpha}^{(1)}) P_{\uparrow\downarrow} + \hat{D}_{\alpha}(\beta_{\alpha}^{(2)}) P_{\downarrow\uparrow} \right) + P_{\downarrow\downarrow} \left(\hat{D}_{\alpha}(-\beta_{\alpha}^{(2)}) P_{\uparrow\downarrow} + \hat{D}_{\alpha}(-\beta_{\alpha}^{(1)}) P_{\downarrow\uparrow} \right) \right\rangle_m \\ &\quad + ie^{i\Theta^{\uparrow\uparrow}} \left\langle P_{\uparrow\uparrow} \left(\hat{D}_{\alpha}(-\beta_{\alpha}^{(1)}) P_{\uparrow\downarrow} + \hat{D}_{\alpha}(-\beta_{\alpha}^{(2)}) P_{\downarrow\uparrow} \right) + P_{\downarrow\downarrow} \left(\hat{D}_{\alpha}(\beta_{\alpha}^{(2)}) P_{\uparrow\downarrow} + \hat{D}_{\alpha}(\beta_{\alpha}^{(1)}) P_{\downarrow\uparrow} \right) \right\rangle_m \\ &\quad + P_{\uparrow\uparrow}P_{\downarrow\downarrow} \left\langle \hat{D}_{\alpha}(-(\beta_{\alpha}^{(1)} + \beta_{\alpha}^{(2)})) + \hat{D}_{\alpha}(\beta_{\alpha}^{(1)} + \beta_{\alpha}^{(2)}) \right\rangle_m \\ &\quad + P_{\uparrow\downarrow}P_{\downarrow\uparrow} \left\langle \hat{D}_{\alpha}(\beta_{\alpha}^{(1)} - \beta_{\alpha}^{(2)}) + \hat{D}_{\alpha}(\beta_{\alpha}^{(2)} - \beta_{\alpha}^{(1)}) \right\rangle_m. \end{aligned} \quad (\text{S44})$$

To evaluate the trace over the motional degrees of freedom, we assume an initial thermal product state at temperature T :

$$\hat{\rho}_m = \bigotimes_{\alpha} \left(1 - e^{-\hbar\omega_{\alpha}/(k_B T)}\right) \sum_{n=0}^{\infty} |n\rangle \langle n| e^{-n\hbar\omega_{\alpha}/(k_B T)}. \quad (\text{S45})$$

From this state, we can compute the thermal expectation value of products of displacement operators on each mode, i.e.

$$\left\langle \prod_{\alpha} \hat{D}_{\alpha}(\beta_{\alpha}) \right\rangle_m = \exp \left\{ - \sum_{\alpha} |\beta_{\alpha}|^2 \left(\bar{n}_{\alpha} + \frac{1}{2} \right) \right\}, \quad (\text{S46})$$

with $\bar{n}_{\alpha} = \coth(\hbar\omega_{\alpha}/(k_B T)) - 1/2$ giving the average phonon occupation of the α -th mode. Using this result, we can then express the state-dependent fidelity as:

$$\begin{aligned} \mathcal{F}_{|\psi_0\rangle} &= 2P_{\uparrow\uparrow} \left(P_{\uparrow\downarrow} \cos(2\Delta\Phi) e^{-\sum_{\alpha} (\bar{n}_{\alpha} + 1/2) |\beta_{\alpha}^{(1)}|^2} + P_{\downarrow\uparrow} \cos(2\Delta\Phi) e^{-\sum_{\alpha} (\bar{n}_{\alpha} + 1/2) |\beta_{\alpha}^{(2)}|^2} + P_{\downarrow\downarrow} e^{-\sum_{\alpha} (\bar{n}_{\alpha} + 1/2) |\beta_{\alpha}^{(1)} + \beta_{\alpha}^{(2)}|^2} \right) \\ &\quad + 2P_{\uparrow\downarrow} \left(P_{\downarrow\uparrow} e^{-\sum_{\alpha} (\bar{n}_{\alpha} + 1/2) |\beta_{\alpha}^{(1)} - \beta_{\alpha}^{(2)}|^2} + P_{\downarrow\downarrow} \cos(2\Delta\Phi) e^{-\sum_{\alpha} (\bar{n}_{\alpha} + 1/2) |\beta_{\alpha}^{(2)}|^2} \right) \\ &\quad + 2P_{\downarrow\uparrow}P_{\downarrow\downarrow} \cos(2\Delta\Phi) e^{-\sum_{\alpha} (\bar{n}_{\alpha} + 1/2) |\beta_{\alpha}^{(2)}|^2} + 1. \end{aligned} \quad (\text{S47})$$

Here we have defined the error in the relative phase:

$$\Delta\Phi \equiv \left| \frac{\Theta^{\uparrow\uparrow} - \Theta^{\downarrow\downarrow}}{2} \right| - \frac{\pi}{4}, \quad (\text{S48})$$

such that when $\Delta\Phi = 0$, and the motional states are perfectly restored (i.e. $\beta_\alpha^{(i)} = 0$), the ideal unitary \hat{U}_{id} is implemented up to global phase – i.e. $\mathcal{F} = 1$.

We may then obtain the state-averaged fidelity for the two-qubit state by integrating over the surface of the 3-sphere spanned by the probabilities P_{ij} – noting that the relative phases between the two-qubit states do not contribute to the fidelity expression. This is achieved by the use of hyperspherical coordinates for the coefficients of each of the two-qubit states, which gives

$$P_{\downarrow\downarrow} = \cos^2(\theta_1), \quad (\text{S49a})$$

$$P_{\downarrow\uparrow} = \sin^2(\theta_1) \cos^2(\theta_2), \quad (\text{S49b})$$

$$P_{\uparrow\downarrow} = \sin^2(\theta_1) \sin^2(\theta_2) \cos^2(\theta_3), \quad (\text{S49c})$$

$$P_{\uparrow\uparrow} = \sin^2(\theta_1) \sin^2(\theta_2) \sin^2(\theta_3), \quad (\text{S49d})$$

where $0 < \Theta_{1,2} < \pi$, and $0 \leq \theta_3 < 2\pi$. The state-averaged fidelity, \mathcal{F}_{av} , is then given by integrating Eq. (S47) over all angles:

$$\mathcal{F}_{\text{av}} = \frac{\int_0^\pi d\theta_1 \int_0^\pi d\theta_2 \int_0^{2\pi} d\theta_3 \sin^2(\theta_1) \sin(\theta_2) \mathcal{F}_{|\psi_0\rangle}[\theta_1, \theta_2, \theta_3]}{\int_0^\pi d\theta_1 \int_0^\pi d\theta_2 \int_0^{2\pi} d\theta_3 \sin^2(\theta_1) \sin(\theta_2)}, \quad (\text{S50})$$

$$\begin{aligned} &= \frac{1}{2} + \frac{\cos(2\Delta\Phi)}{6} \left(e^{-\sum_\alpha (\bar{n}_\alpha + 1/2) |\beta_\alpha^{(1)}|^2} + e^{-\sum_\alpha (\bar{n}_\alpha + 1/2) |\beta_\alpha^{(2)}|^2} \right) \\ &+ \frac{1}{12} \left(e^{-\sum_\alpha (\bar{n}_\alpha + 1/2) |\beta_\alpha^{(1)} - \beta_\alpha^{(2)}|^2} + e^{-\sum_\alpha (\bar{n}_\alpha + 1/2) |\beta_\alpha^{(1)} + \beta_\alpha^{(2)}|^2} \right). \end{aligned} \quad (\text{S51})$$

As we are interested in small errors, we may expand the above expression to leading order in $\Delta\Phi$ and $\{|\beta_\alpha^{(i)}|\}$ to obtain a simple expression for the infidelity. We perform this expansion in terms of the centre-of-mass and relative coordinates for the motional state amplitudes, by substituting

$$\beta_\alpha^{(1),(2)} = \beta_\alpha^- \pm \beta_\alpha^+ \quad (\text{S52})$$

into Eq. (S51), and then taking the series expansion to give:

$$1 - \mathcal{F}_{\text{av}} \approx \frac{2|\Delta\Phi|^2}{3} + \frac{2}{3} \sum_\alpha \left(\bar{n}_\alpha + \frac{1}{2} \right) (|\beta_\alpha^+|^2 + |\beta_\alpha^-|^2), \quad (\text{S53})$$

which gives Eq. (3) of the main text. As a consistency check, we can consider the special case of a same-species crystal for which $\eta_\alpha^+ = \eta_\alpha^- \equiv \eta_\alpha$:

$$1 - \mathcal{F}_{\text{av}} \approx \frac{2|\Delta\Phi|^2}{3} + \frac{2}{3} \sum_\alpha \left(\bar{n}_\alpha + \frac{1}{2} \right) (|\beta_\alpha^+|^2 + |\beta_\alpha^-|^2), \quad (\text{S54})$$

$$= \frac{2|\Delta\Phi|^2}{3} + \frac{4}{3} \sum_\alpha \left(\bar{n}_\alpha + \frac{1}{2} \right) \left[(b_\alpha^{(1)})^2 + (b_\alpha^{(2)})^2 \right] \left| 2\eta_\alpha \sum_k z_k e^{i\omega_\alpha t_k} \right|^2, \quad (\text{S55})$$

which is precisely the result employed in Refs. [27–33].

(3) Additional error analysis

In Figure 1(e) of the main text, we studied the effect of SDK timing jitter on select MHz-speed gates for the ion pairs ^{133}Ba – ^{138}Ba and ^{43}Ca – ^{88}Sr . Figure [S1] provides a broader dataset that describes the effect of SDK timing jitter on gates between the dual-isotopes pair ^{43}Ca – ^{40}Ca and the large mass-imbalance pair ^{171}Yb – ^7Be . The results are quantitatively and qualitatively similar to those discussed in the main text: subnanosecond timing control is sufficient to ensure gate errors of $\sim 10^{-4}$, for all ion pairs and gate speeds studied.

Figure [S2] similarly supplements Fig. 1(f) of the main text, wherein the impact of shifts in the frequency of the out-of-phase (op) mode is studied. The results are consistent across all four ion pairings studied: mode dependent shifts of 0.1% (1%) contribute gate errors of roughly 10^{-4} (10^{-2}) across all ion pairings and gate speeds studied.

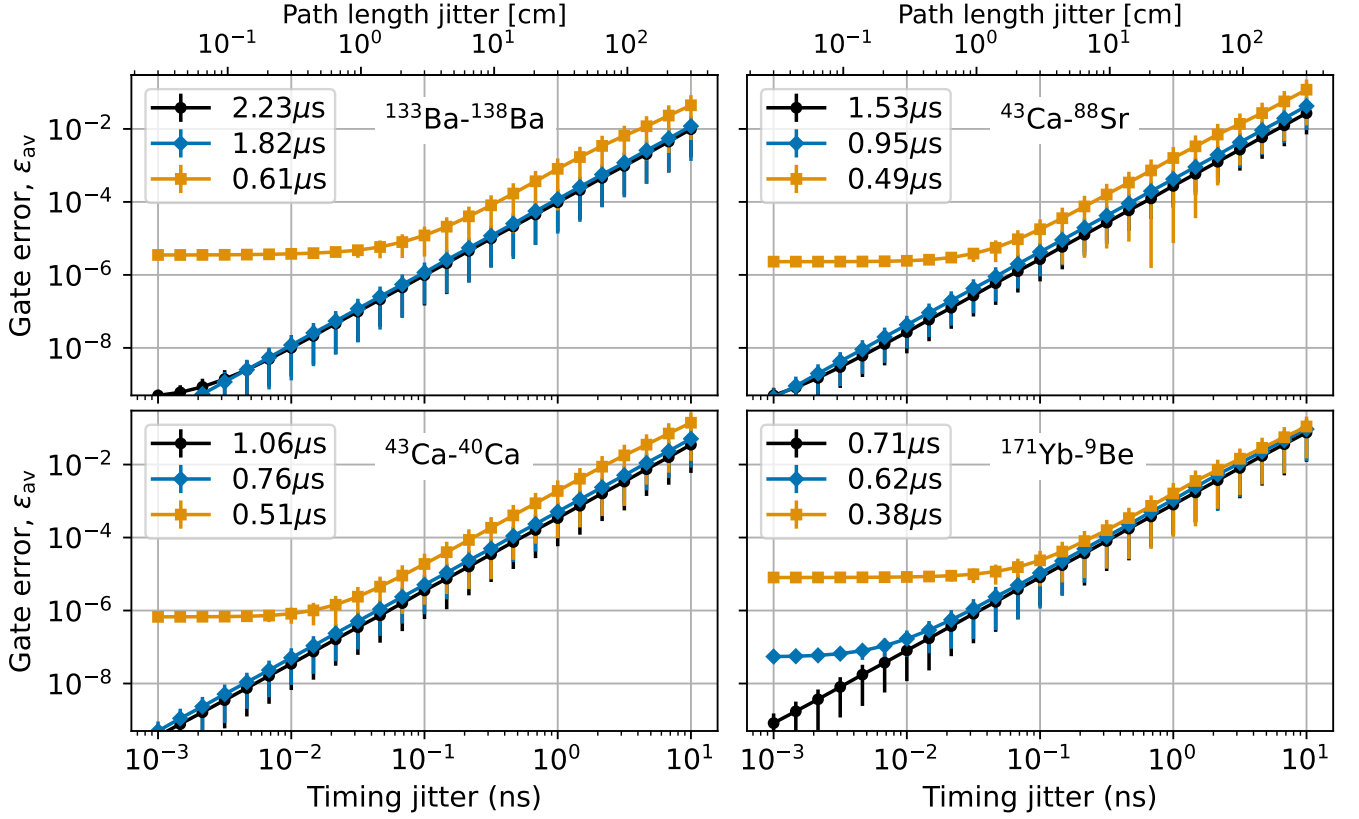


FIG. [S1]. Sensitivity of MHz-speed gate solutions against timing jitter in the SDK pulse sequence, with the gate error averaged over 10^4 noise realisations. Errorbars indicate the standard deviation in the ensemble average.

Figure [S3] presents results describing the degradation of gate fidelity under frequency shifts common to both modes, which is both qualitatively and quantitatively similar to the results in Fig. [S2] – high-fidelity gate realisations require stabilisation of the trapping frequencies at the 0.1% level, which translates to shifts of about 10kHz for a 1MHz secular trapping frequency.

Lastly, we consider an error model to describe the gate error induced by drifts in the effective SDK repetition rate away from the 200MHz SDK train bandwidth assumed in the main text. This error model is distinct to the effects of timing jitter as only the relative timings of SDKs separated by a single repetition period are modified – this is treated as a systematic shift, rather than a random error. Fig. [S4] demonstrates that gate solutions around $1\mu\text{s}$ typically have SDKs separated by many repetition periods (10 – 100ns) and are thus entirely unaffected by drifts in the SDK repetition rate. We find that only gate solutions much faster than the trapping period, i.e. $\tau_G \ll 1\mu\text{s}$, are affected by drifts in the SDK repetition rate, although large drifts of at least 10% are required to contribute gate errors above 10^{-4} . Interestingly, tuning the repetition rate by a few percent can improve the gate fidelity for some gate solutions.

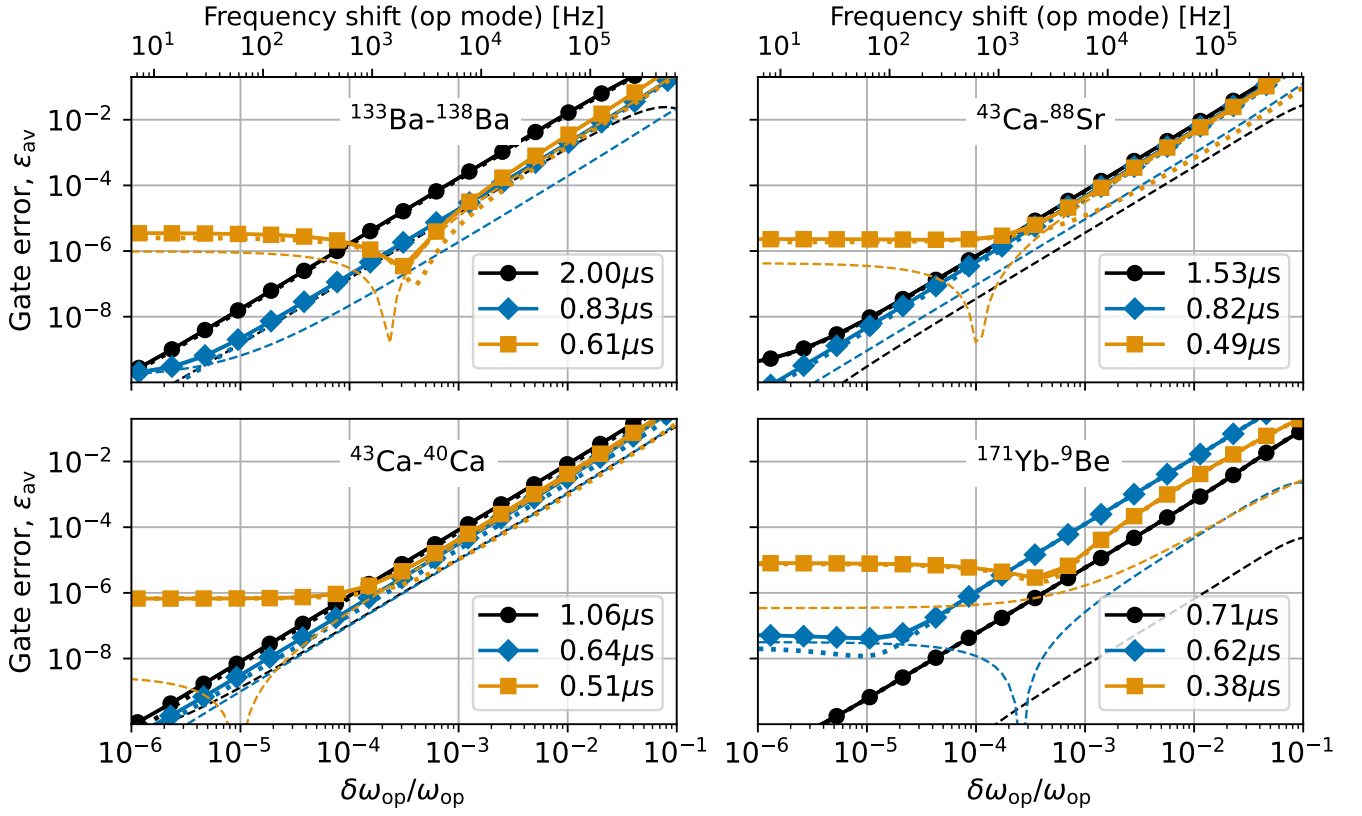


FIG. [S2]. Effect of frequency drift on the out-of-phase ('op') motional mode, for a range of gate times. Dashed (dotted) lines indicates contribution of phase (motional) errors to the total gate infidelity given by Eq. (S53).

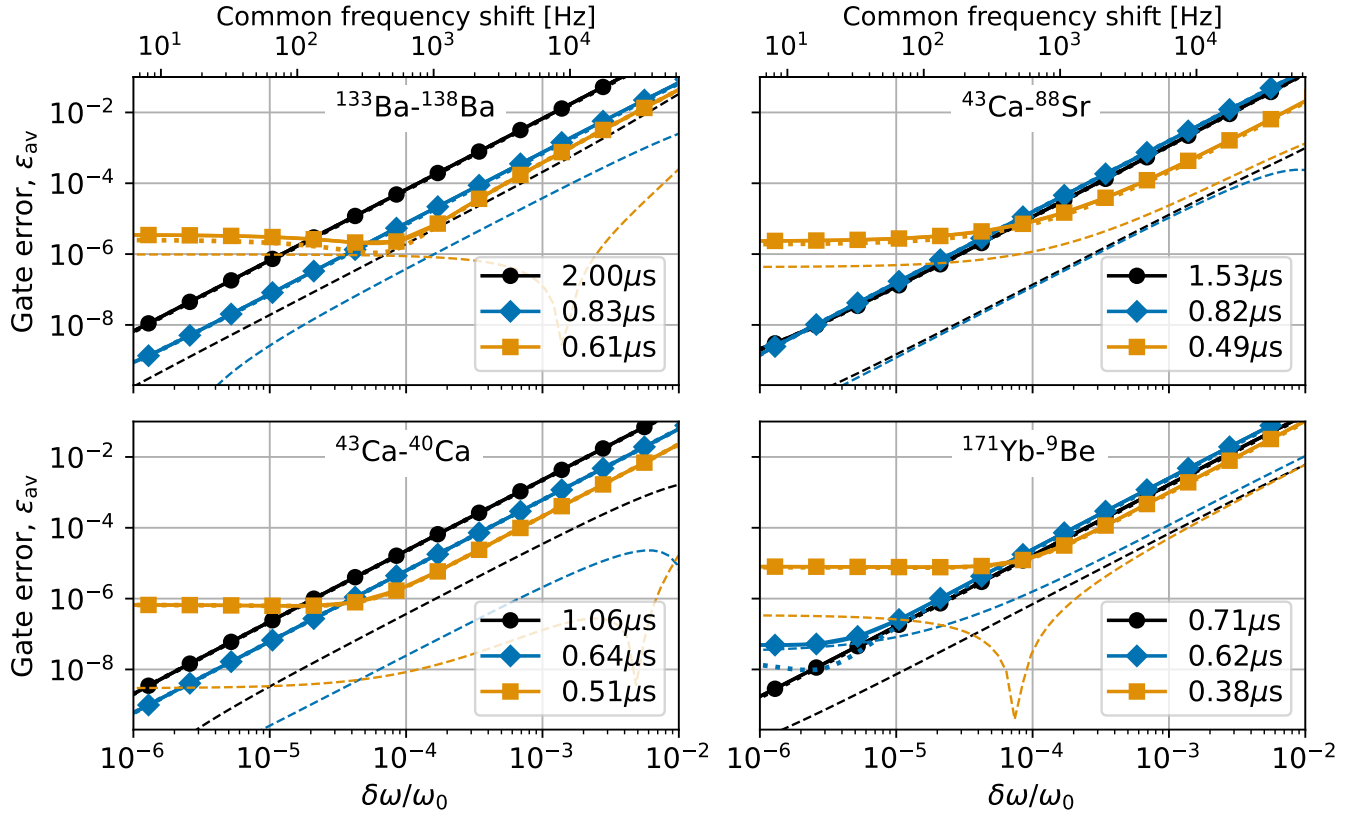


FIG. [S3]. Effect of frequency drifts common to both motional modes, for a range of gate times. Dashed (dotted) lines indicates contribution of phase (motional) errors to the total gate infidelity given by Eq. (S53).

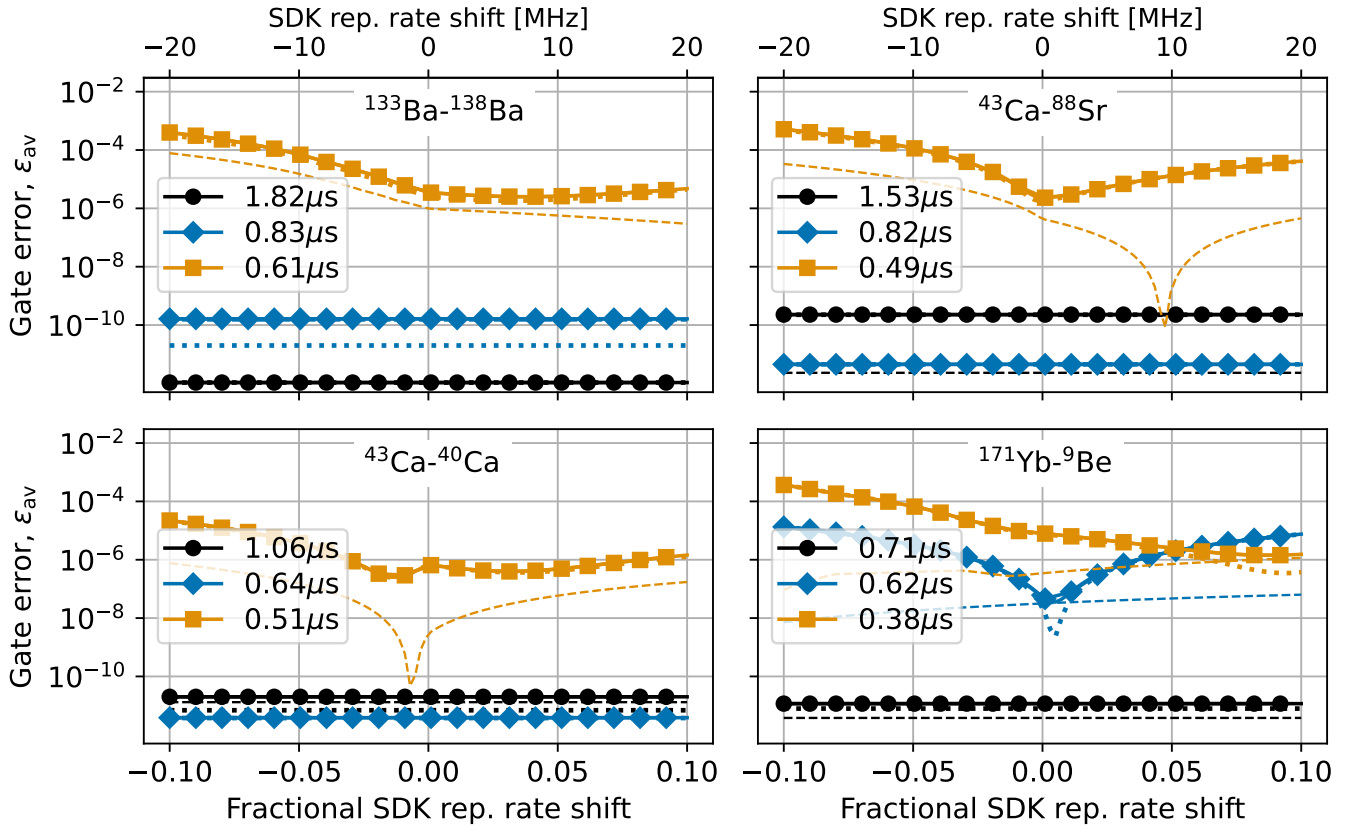


FIG. [S4]. Effect of drifts or miscalibrations of the SDK repetition rate for gate solutions designed for a 200MHz SDK bandwidth, for a range of gate times. Dashed (dotted) lines indicates contribution of phase (motional) errors to the total gate infidelity given by Eq. (S53).